Experimental Thermal and Fluid Science 98 (2018) 362–368

Contents lists available at ScienceDirect

Experimental Thermal and Fluid Science

journal homepage: www.elsevier.com/locate/etfs

Study on coalescence dynamics of unequal-sized microbubbles captive on solid substrate

Shuyi Zhou[a], Yuanzhi Cao[a], Rou Chen[a], Tao Sun[b], Kamel Fezzaa[b], Huidan Yu[a], Likun Zhu[a,*]

[a] Department of Mechanical Engineering, Indiana University–Purdue University Indianapolis, Indianapolis, IN 46202, USA
[b] Advanced Photon Source, Argonne National Laboratory, Argonne, IL 60439, USA

ARTICLE INFO

Keywords:
Bubble coalescence
Synchrotron
High-speed X-ray imaging
Bridging neck growth
Surface wave propagation
Microfluidic

ABSTRACT

The dynamics of bubble coalescence are of importance for a number of industrial processes, in which the size inequality of the parent bubbles plays a significant role in mass transport, topological change and overall motion. In this study, coalescence of unequal-sized microbubbles captive on a solid substrate was observed from cross-section view using synchrotron high-speed imaging technique and a microfluidic gas generation device. The bridging neck growth and surface wave propagation at the early stage of coalescence were investigated by experimental and numerical methods. The results show that theoretical half-power-law of neck growth rate is still valid when viscous effect is neglected. However, the inertial-capillary time scale is associated with the initial radius of the smaller parent microbubble. The surface wave propagation rate on the larger parent microbubble is proportional to the inertial-capillary time scale.

1. Introduction

Coalescence of microbubbles are encountered in many industrial applications when gas microbubbles are generated from or injected into liquid reactants, such as solar water splitting systems [1–3], microbial electrolysis cells [4–6], and gas-liquid synthesis [7–9]. Fundamental understanding of coalescence dynamics of microbubbles is essential to the design of those systems and devices. To this end, most studies on microbubble coalescence have been focused on equal-sized parent bubbles with a complete spherical shape. For instance, the dynamics of thinning and rupture of the liquid film between two approaching bubbles just prior to coalescence have been studied extensively [10–14]. The dynamics of bridging neck growth have been the focus of many studies [15–19]. It has been shown that the bridging neck radius r of two parent bubbles follows a power-law, $r/R \propto (t/\tau)^{1/2}$, at the early-stage of coalescence, where R is the initial radius of parent bubbles and τ is a time scale. When viscous effect is negligible, the time scale is inertial-capillary time scale $\tau = (\rho R^3/\sigma)^{1/2}$, where ρ is the density of liquid and σ is the surface tension [17]. Stover et al. investigated the effects of bubble size, electrolyte viscosity, and surface tension on the oscillation dynamics of a coalesced bubble [20]. They found that fluid inertia sustains the oscillation of the resultant bubble and viscous resistance dampens the oscillation. The oscillation period increases and damping decreases with increasing bubble size. Within the viscosity range from 1.1×10^{-2} cm^2/s to 5.0×10^{-2} cm^2/s, the oscillation frequency is insensitive to the viscosity and damping is insensitive to surface tension. Coalescence does not depend on gas type or electrolyte pH. These studies using equal-sized spherical bubbles have provided useful information on the dynamics of microbubble coalescence. However, in real applications, coalescence could happen when microbubbles are captive on a solid substrate with a spherical segment shape. In addition, the parent bubble sizes are different for most of the coalescence cases. Recently, Weon et al. have reported that the location of the coalesced bubble is linked by the parent bubble size ratio with a power-law relationship [21,22]. Chen et al. reported that the coalescence time also exhibits a power-law scaling with the parent bubble size ratio [23]. Zhang et al. studied the generation of a satellite during the coalescence of two gas bubbles. They found that the relative size of the parent bubbles has a critical effect on the generation of satellite, preventing it if this ratio is too large or too small [24]. However, the dynamics in the early-stage of coalescence of two unequal-sized microbubbles captive on a solid substrate have not been studied. The objective of this paper is to investigate whether there exists a universal time scaling law in such coalescence cases. In this study, the coalescence of two unequal-sized microbubbles captive on a solid substrate was investigated experimentally and numerically. A polymer microfluidic device was designed and fabricated to generate microbubbles and bubble coalescence events. A high-speed X-ray imaging instrument

* Corresponding author at: Department of Mechanical Engineering, Indiana University Purdue University Indianapolis, 723 W. Michigan Street, Room SL 260 L, Indianapolis, IN 46202, USA.
E-mail address: likzhu@iupui.edu (L. Zhu).

https://doi.org/10.1016/j.expthermflusci.2018.06.016
Received 28 September 2017; Received in revised form 2 May 2018; Accepted 20 June 2018
Available online 21 June 2018

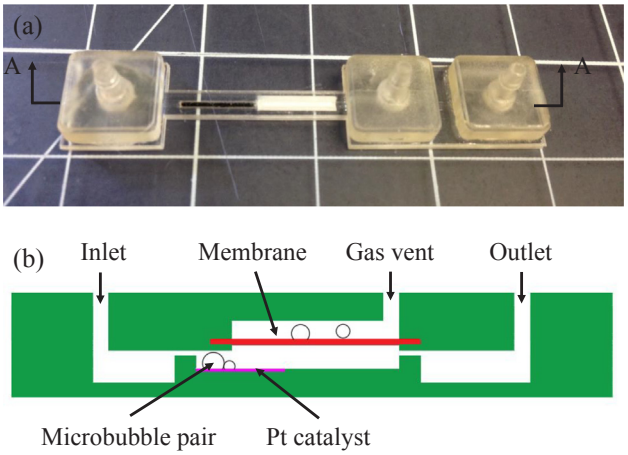

Fig. 1. (a) A picture of the fabricated polymer microfluidic gas generation device and (b) schematic of the cross-section view of the device.

at the 32-ID-B beamline of the Advanced Photon Source (APS) at Argonne National Laboratory was used to visualize individual coalescence events inside the polymer microfluidic channel. The bridging neck growth and surface wave propagation at the early stage of bubble coalescence were analyzed based on the X-ray images and simulation results.

2. Experimental

The coalescence experiment was carried out through microbubbles generated inside a polymer microfluidic gas generation device. The device was fabricated by aligning and sequentially stacking/thermo-press bonding multiple layers of patterned polystyrene (PS) film (Goodfellow, Coraopolis, PA) which were achieved by a craft cutter (FC2250-60 VC, Graphtec, Santa Ana, CA) [25]. A picture of the device and the schematic of a cross-section view of the device are shown in Fig. 1. A reaction microchannel was formed by bonding a platinum (Pt) black catalyst layer inside the microchannel. The Pt black was electroplated on a gold foil (10 μm thick) with 0.1 A/cm^2 current density for 55 s. The plating bath consisted of 120 ml of DI water and 5 g of dihydrogen hexachloroplatinate ($H_2PtCl_6{\cdot}6H_2O$, Alfa AESAR, Ward Hill, MA) [26]. The Pt density was measured and calculated to be 1.5 mg/cm^2. The gold foil was attached on a double-sided tape when being electroplated with Pt. Then it can be attached to PS film with the other adhesive surface, as is shown in Fig. 1(b). In order to vent the gas bubble in the reaction channel, a hydrophobic nanoporous membrane (0.2 μm pore size, Sterlitech Corporation, Kent, WA) was embedded into the device, as is shown in Fig. 1(b).

High-speed X-ray imaging experiments were conducted at the 32-ID-B beamline of APS to visualize individual coalescence events in the reaction channel. The experimental setup is illustrated in Fig. 2(a). An intense undulator white-beam went through the reaction channel of the device and generated phase-contrast images of the sample. A LuAG:Ce scintillator (100 μm thickness), positioned downstream, absorbed the X-ray photons and emitted visible light, which was then recorded by a high-speed camera (FastCam SA1.1, Photron) with 10^5 fps and 3 μs exposure time, as is shown in Fig. 2(b). It should be noted that the coalescence events were visualized from the cross-section view in this study. Since the parent microbubbles were captive on the Pt catalyst substrate with 36° contact angle, the top view cannot reveal the detailed dynamic information of bubble coalescence. In order to gain better image contrast, the longitudinal dimension of the reaction channel should be as small as possible to reduce the X-ray absorption by channel walls and liquid reactant, as is shown in Fig. 2(c). In this study, the rectangular reaction channel width was 0.7 mm with 1.15 mm PS wall on each side and the channel height was 144 μm. 30% hydrogen peroxide (H_2O_2) was used as reactant solution in this experiment. Oxygen generation reaction happened when the H_2O_2 solution was brought into contact with the Pt catalyst inside the reaction channel. To avoid the influence of X-ray on H_2O_2, we optimized the X-ray dose to make sure H_2O_2 didn't have obvious self-reaction under existence of the X-ray while the contrast of the image remained clear. As shown in Fig. 2(e), the phase-contrast X-ray image clearly shows the profiles of microbubbles and other substances with 2 μm spatial resolution.

The measurement of bridging neck growth and surface wave propagation based on X-ray images was aided by open software, ImageJ (National Institutes of Health). The detailed information about image processing and measurement uncertainty is shown in Fig. 3. As shown in Fig. 3a, the bubble center locations were determined before the bubbles started coalescence. Since the bubbles were at equilibrium before coalescence, their 3D shape should be perfect spherical segment and their 2D projection images shown in Fig. 3a should be perfect circular segment. To determine the location of the center, we have to find the boundary of the circular segment. As shown in Fig. 3b and c, a median filter in ImageJ (Despeckle) was used to remove the salt and pepper noise by replacing each pixel with the median value in its 3 × 3 neighborhood. Fig. 3d shows the gray value profile along the solid line shown in Fig. 3c. We selected the pixel with the lowest gray value to be the boundary. After the boundary of the circular segment was determined, the center can be determined. Since the pixel size is 2 μm in this study, the uncertainty of the center location is 2 μm.

3. Results and discussion

The high-speed synchrotron X-ray imaging technique allowed the direct observation of the captive microbubble coalescence inside the reaction channel from the cross-section view, due to the small wavelengths of hard X-rays (~0.1 nm) [27]. In addition, this microfluidic gas generator enables the cross-section view of captive bubbles on the solid substrate. Fig. 4 shows an example of the coalescence of two unequal-sized microbubbles. The whole coalescence process took place in 170 μs. A series of images have been taken by the high-speed camera at a frame rate of 10^5 fps. Since H_2O_2 solution had flow motions inside the reaction channel and oxygen generation took place continuously during the imaging process, it is necessary to identify whether the flow motion and oxygen generation had impact on the individual coalescence event. It can be seen from the images in Fig. 4 that all other bubbles do not have clear change during the 170 μs time span. Therefore, we can conclude that the flow motion and oxygen generation were at a relatively low speed and they don't have impact on individual coalescence event. In Fig. 4 at 0 μs, two microbubbles, with radius 64 μm and 36 μm respectively, were about to contact each other. The coalescence of the two microbubbles took place in a very short period of time and in the next frame at 10 μs, the two microbubbles have formed a bridging neck, with an arch shape in the middle. It should be noted that the coalescence events were selected from the video of gas generation in the microchannel. In this experiment, the start of a coalescence event cannot be controlled. Since the temporal resolution of the high-speed camera was 10 μs, the uncertainty in determining the initial time (0 μs) was 10 μs. 10 μs uncertainty is relative large for this study. In order to address this issue, the experimental results and simulation results were compared when selecting the coalescence events and determining the initial time. As show in Fig. 5, the simulation results show similar time as the experimental when they have the similar neck growth. From 10 μs to 60 μs, it is observed that a surface wave on the liquid-gas interface travels on the larger bubble. During this period, the

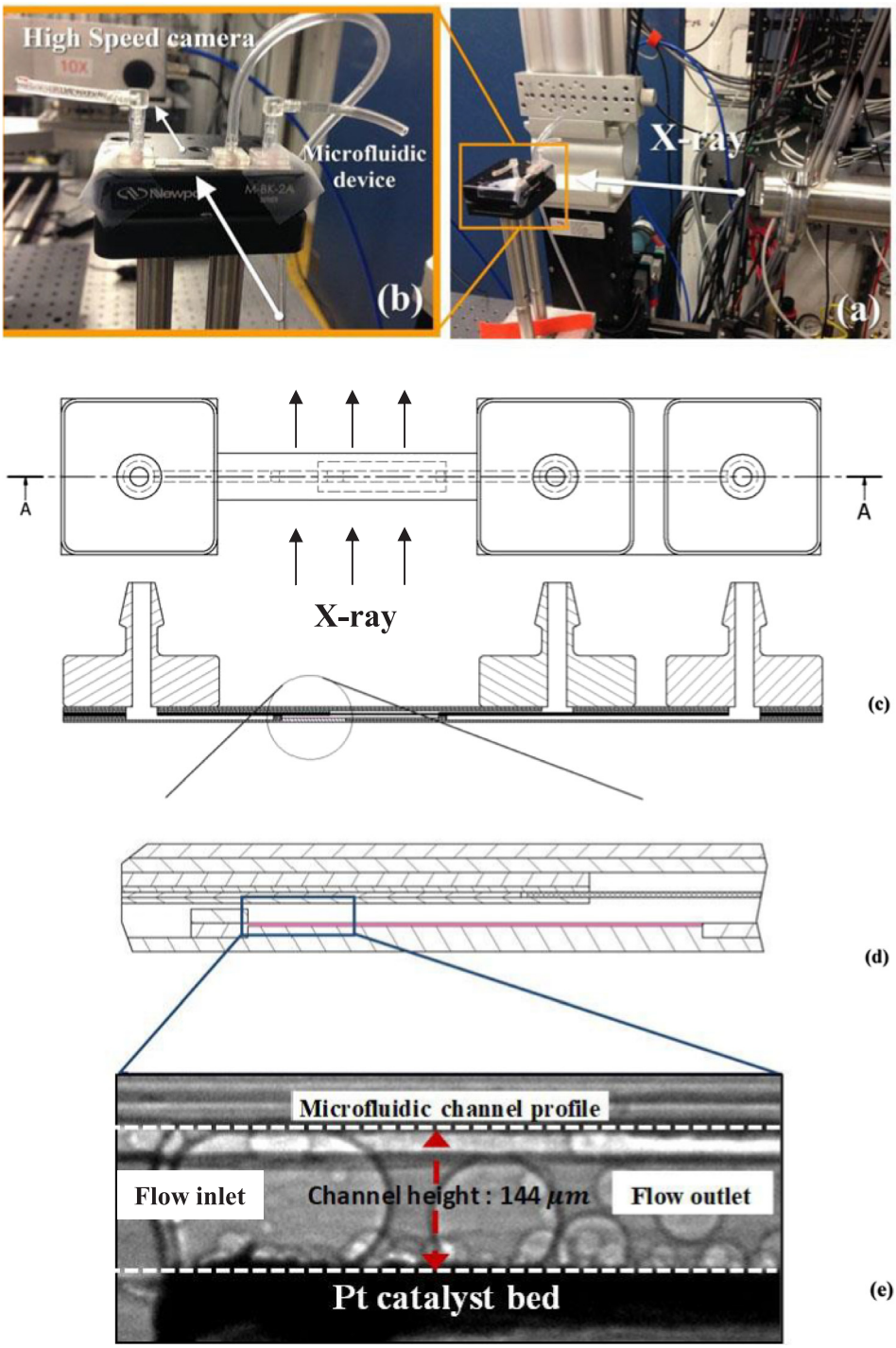

Fig. 2. (a, b) X-ray high-speed imaging experiment setup. (c) Schematic of the gas generation device. (d) Detailed view of the reaction channel. (e) Phase contrast image of a microbubble pair.

shape of the coalesced microbubble shows significant dynamic change. From 70 μs to 170 μs, the coalesced bubble does not show large shape change and slowly restored the spherical segment shape with 36° contact angle at 170 μs.

As shown in Fig. 4, when two separate microbubbles contacted each other, the formation of a bridge occurred and the bridge neck grew rapidly at the early stage of coalescence. The measurement of the neck radius for equal-sized microbubble pair is a distance from the middle point in the center line through two parent microbubbles to the saddle point of the merged surface. The determination of neck radius for unequal-sized microbubble pair is more complex than the same size pair. The neck radius is the perpendicular distance from the saddle point of the merged surface to the line through two parent microbubble centers, as is shown in Fig. 6(a).

Previous studies have shown that the neck radius r of equal-sized bubbles follows a power-law, $r/R \propto (t/\tau)^{1/2}$, at the early stage of

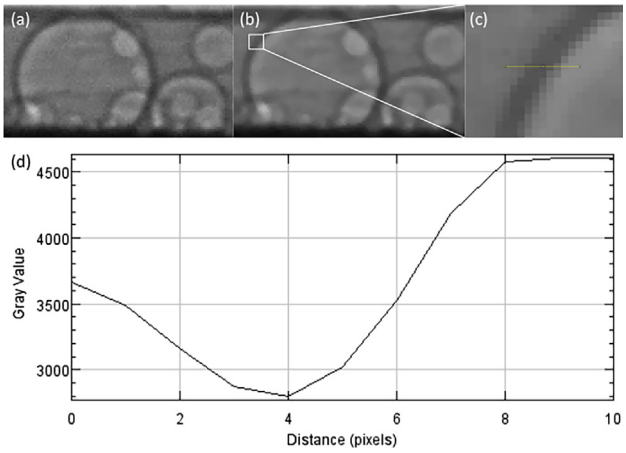

Fig. 3. (a) Original image of the unequal-sized microbubble coalescence event at time 0 μs shown in Fig. 4. (b) The processed image after a median filter in ImageJ (Despeckle) was used to remove the salt and pepper noise. (c) Boundary of the circular segment. (d) Gray value profile along the solid line shown in (c).

coalescence. $\tau = (\rho R^3/\sigma)^{1/2}$ is inertial-capillary time scale, when viscous effect is negligible [17]. In this study, coalescence dynamics of unequal-sized microbubbles was investigated and we want to answer the following three questions. (1) Does a universal power law exist for the bridging neck growth? (2) Does the size ratio have an impact on the neck growth dynamics? (3) What is the characteristic length in the unequal-sized case? Since the Ohnesorge (Oh) number ($Oh = \mu/(\rho\sigma L)^{1/2}$),a dimensionless number that relates the viscous force to inertial and surface tension forces, was about 0.01 in this experiment, we can consider that the viscous effect is negligible. Three individual coalescence events were selected for this study with radius ratios of the two microbubbles 1.02 (56 μm and 55 μm), 1.45 (42 μm and 29 μm), and 1.78 (64 μm and 36 μm), respectively. It was considered that the bridging neck growth process was complete when the neck radius was the same as the radius of smaller parent microbubble. If the radius of the smaller microbubble (R_s) was chosen as the characteristic length, the dash fitting line in Fig. 7 shows that the neck growth evolution follows a half power-law at the early stage of coalescence, r/R_s $1.38(t/\tau_s)^{\frac{1}{2}}$, $\tau_s = (\rho R_s^3/\sigma)^{\frac{1}{2}}$, with coefficient of determination $R^2 = 0.9709$. However, due to the extremely fast evolution of bridging neck, the high-speed camera with 10^5 fps only can capture one or two points for those three cases. As shown in Fig. 7, there are four points in total. In order to obtain more data points, we conducted 3D simulation in the same conditions, including microbubble and solution properties, surface tension, contact angle, size ratio etc. using commercial CFD software FLUENT 16.0 (ANSYS, Inc., 2014). The multiphase 3D Volume of Fluid model in FLUENT was used in the simulation. The pre-processor GAMBIT in FLUENT was used to form the computational geometry and grids. The convergence of different mesh size was tested. 3D hexahedron shape and mesh edge of 1 μm modeling gave a smooth appearance of microbubble, especially dealing with solid interface and time-saving. For multi-zone design, specified area with much smaller size mesh resulted in same phenomena but longer simulating time. Hence, hex element with mesh edge of 1 μm was generated for the cuboid with$250\mu m(X) \times 200\mu m(Y) \times 200\mu m(Z)$. Periodic boundary was imposed into the Z and X direction with 50,000 and 40,000 quadrilateral faces respectively. The top and bottom faces in the Y direction were set as wall adhesion with the contact angle $\alpha = 36°$ with 50,000 quadrilateral faces. Density of H_2O_2 solution was 1060 kg/m^3 and its viscosity was 1.06 mPa·s, Surface tension coefficient was 0.073 N/m. Density of O_2 was 1.30 kg/m^3, and viscosity of O_2 was 1.92e − 02 mPa·s. The initial position was that two microbubbles were in touch as shown in Fig. 4 at 0 μs. We took Region Adaption to refine the mesh for bubbles. Variable Time Stepping Method was used and the initial time step size was set as 0.1 μs. Due to the spatial and temporal resolution of the imaging technique, the calescence of larger size ratio cases cannot be detected. In addition to the three size ratios obtained from experiment, another 3 size ratios 3 (69 μm and 23 μm), 5 (70 μm and 14 μm) and 10 (70 μm and 7 μm) were simulated. As shown in Fig. 7, the neck growth data from simulation is validated by the four experimental data points. With more data points from simulation, the neck growth still shows a half power-law, r/R_s $1.42(t/\tau_s)^{1/2}$, with coefficient of determination $R^2 = 0.9837$. We can conclude that the neck growth dynamics of two unequal-sized microbubbles captive on a solid surface still shows a half power-law with the inertial-capillary time scale and controlled by the smaller microbubble regardless the size ratio.

As shown in Fig. 4, a surface wave started to propagate along the surface of gas bubble at the initial stage of coalescence. The surface wave was driven by the release of surface energy at the neck region. Wave propagation angle is a way to determine surface wave propagate along bubble surface. As shown in Fig. 6(b), the propagation angle was measured from the line connecting the centers of two parent microbubbles. Since the wave propagation dynamics is very difficult to capture on the smaller parent microbubble, we focused on the surface wave propagation on the larger parent bubble surface. It should be noted that the limit of the surface wave propagation angle was the angle when the wave reached the solid surface. We obtained surface wave propagation angle data on both experiment and simulation with same conditions mentioned in neck growth evolution. If we only consider the experimental results, the solid circular markers show a linear relationship between the propagation angle and the time normalized by inertial-capillary time scale ($\tau_L = (\rho R_L^3/\sigma)^{\frac{1}{2}}$). Since the propagation was on the larger parent microbubble, the characteristic length used in the time scale was the radius of the larger parent microbubble (R_L). The dash fitting line indicates that $\theta = 3.79\left(\frac{t}{\tau_L}\right) + 0.44$, with coefficient of determination $R^2 = 0.9875$. If the simulation results were used, a very similar solid fitting line is present, $\theta = 3.84\left(\frac{t}{\tau_L}\right) + 0.23$, with coefficient of determination $R^2 = 0.9862$. Fig. 8 demonstrates that the surface wave propagation on the larger parent bubble is controlled by the size of larger parent bubble for the unequal-sized case and follows a universal linear relationship with inertial-capillary time scale. However, Fig. 8 also shows that at the very early stage of coalescence the wave propagation does not follow the same linear law as the later stage. The reason could be due to the release of large surface energy at the very early stage when the surface curvature is very large. To explain the surface wave propagation results, a capillary wave theory is used [28]. When the wavelength λ is short, the wave phase velocity v is proportional to $(2\pi\sigma/\rho\lambda)^{1/2}$, where σ is the surface tension, ρ is the density of liquid. In a bubble coalescence event, the capillary wave is the surface wave traveling along the spherical interface of merging bubbles. If we consider that the wavelength is proportional to the radius of the microbubble, the propagation angle $\theta = \frac{vt}{R_l} = t(2\pi\sigma/\rho R_l^3)^{1/2}$. Then $\theta \sim A(\frac{t}{\tau_L})$, where $\tau_L = \sqrt{\frac{\rho R_L^3}{\sigma}}$.

4. Conclusion

We have investigated the neck growth and surface wave propagation at the early stage of coalescence of unequal-sized microbubbles captive on a solid substrate through experiments and CFD simulation. A polymer microfluidic device was designed and fabricated to generate

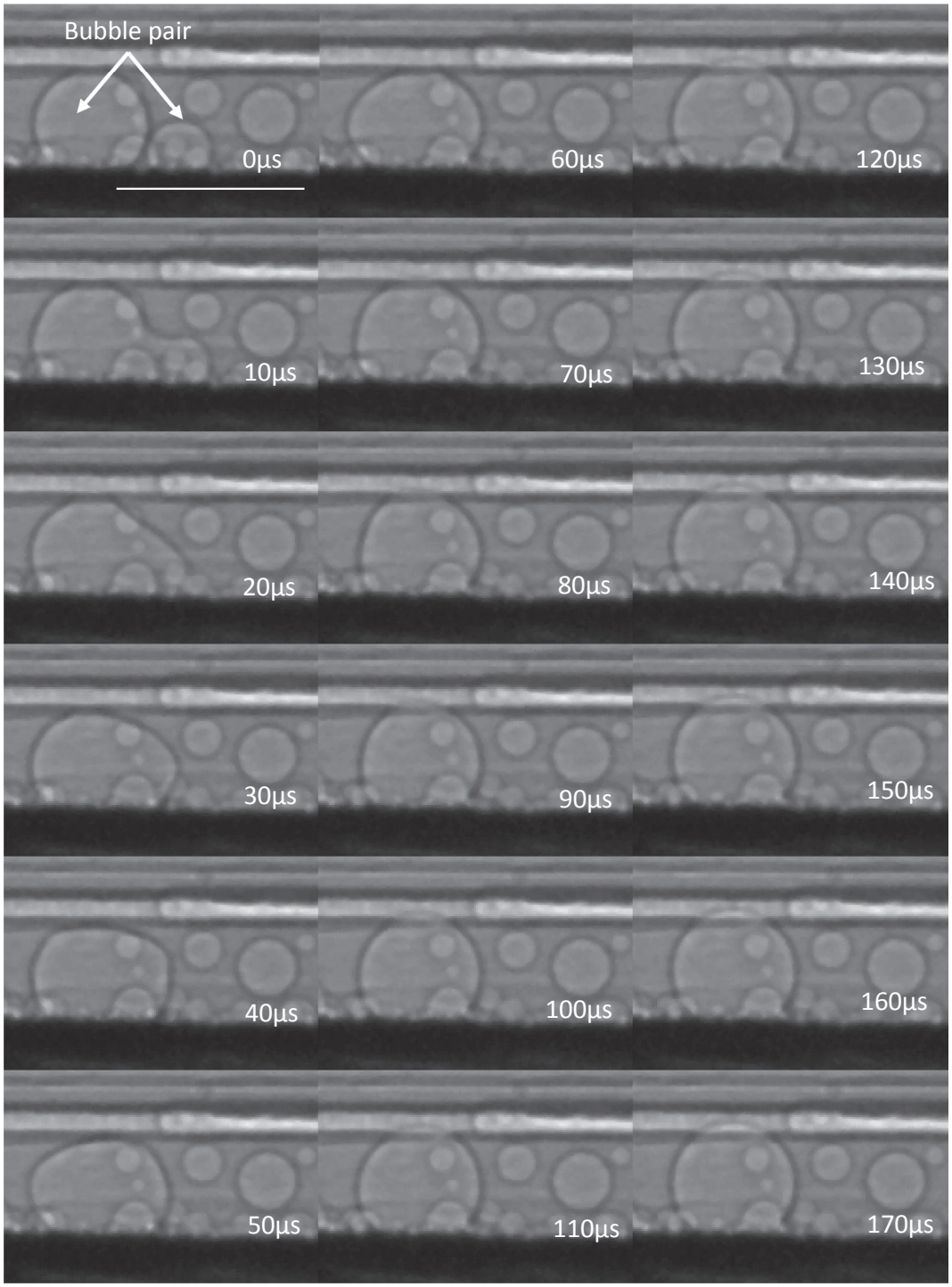

Fig. 4. Representative image sequence of unequal-sized microbubble coalescence. The radii of two parent microbubbles are 64 μm and 36 μm, respectively. The whole coalescence process completed in 170 μs. The scale bar is 200 μm.

microbubbles and coalescence events. The high-speed high-resolution synchrotron X-ray microscopy at the beamline 32-ID-B of the APS was utilized to visualize individual coalescence events in the microchannel from the cross-section view at 10^5 fps frame rate. The image analysis show that the neck growth dynamics of two unequal-sized microbubbles captive on a solid surface shows a half power-law with inertial-capillary time scale and controlled by the smaller parent microbubble. The surface wave propagation on the larger parent microbubble follows a universal linear law with inertial-capillary time scale.

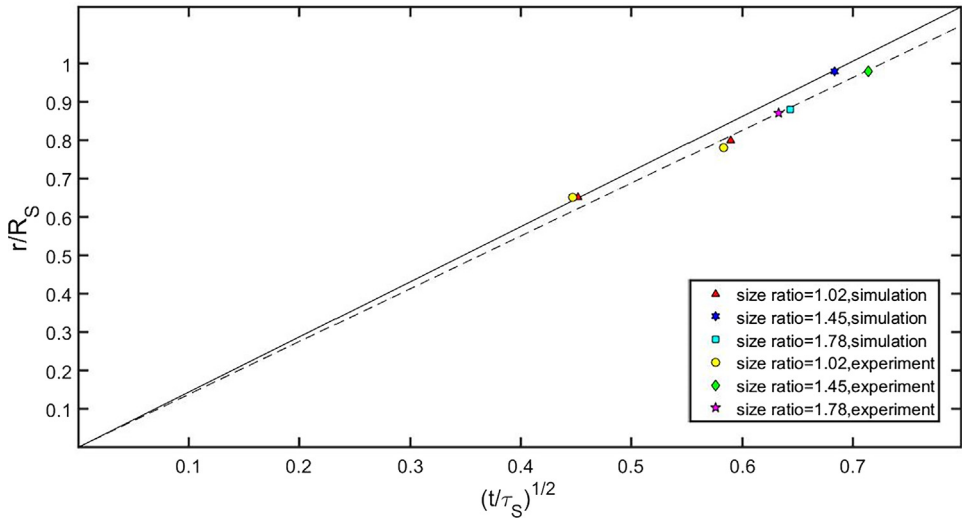

Fig. 5. Comparison between the experimental results of neck growth and the simulation results of neck growth.

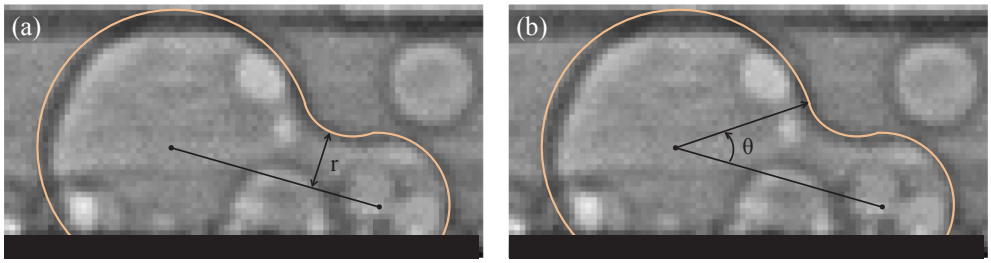

Fig. 6. Schematic of the measurement of (a) bridging neck radius and (b) surface wave propagation angle during coalescence of unequal-sided microbubbles.

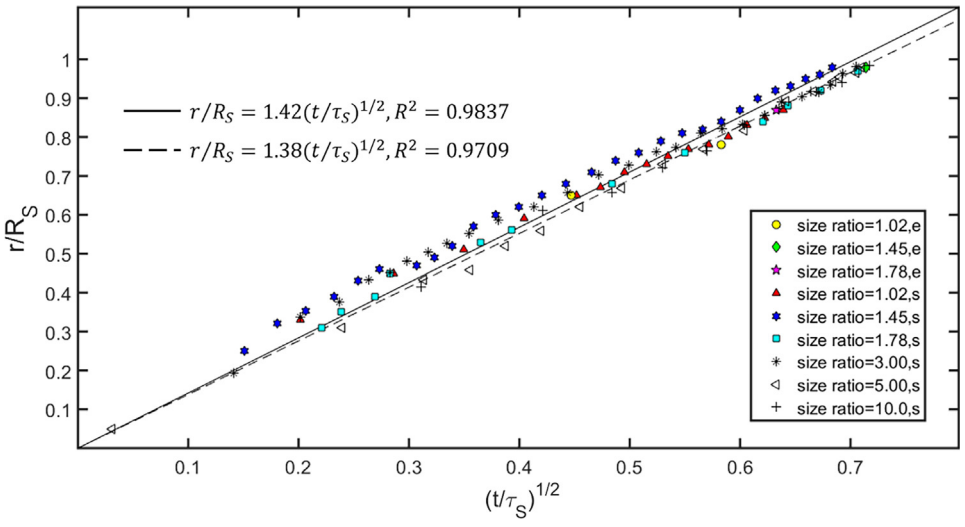

Fig. 7. Time evolution of the bridging neck radius of six coalescence cases with initial radius ratios 1.02 (56 μm and 55 μm), 1.45 (42 μm and 29 μm), 1.78 (64 μm and 36 μm), 3 (69 μm and 23 μm), 5 (70 μm and 14 μm) and 10 (70 μm and 7 μm) obtained from experiment (e) and simulation (s). Dash line and solid line are the fitting lines from experimental results and simulation results, respectively.

Acknowledgment

This material is based upon work supported by the National Science Foundation under Grant No. 1264739 and used resources of the Advanced Photon Source, a U.S. Department of Energy (DOE) Office of Science User Facility operated for the DOE Office of Science by Argonne National Laboratory under Contract No. DE-AC02-06CH11357. We would also like to acknowledge the Integrated Nanosystems Development Institute (INDI) at IUPUI for use of their shared facilities (craft cutter, FESEM, etc.) in support of our research.

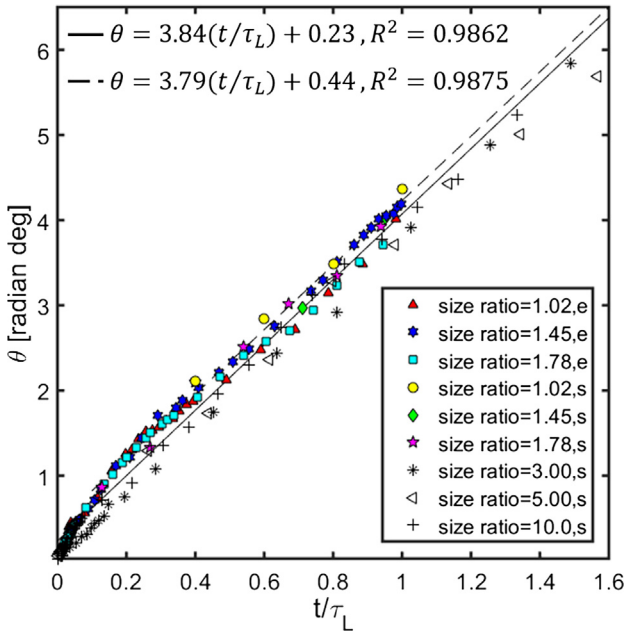

Fig. 8. Time evolution of surface wave propagation angle of six coalescence cases with initial radius ratios 1.02 (56 μm and 55 μm), 1.45 (42 μm and 29 μm), 1.78 (64 μm and 36 μm), 3 (69 μm and 23 μm), 5 (70 μm and 14 μm) and 10 (70 μm and 7 μm) obtained from experiment (e) and simulation (s). Dash line and solid line are the fitting lines from experimental results and simulation results, respectively.

References

[1] E. Selli, G.L. Chiarello, E. Quartarone, P. Mustarelli, I. Rossetti, L. Forni, A photocatalytic water splitting device for separate hydrogen and oxygen evolution, Chem. Commun. (2007) 5022–5024.

[2] M.G. Walter, E.L. Warren, J.R. McKone, S.W. Boettcher, Q. Mi, E.A. Santori, N.S. Lewis, Solar water splitting cells, Chem. Rev. 110 (2010) 6446–6473.

[3] C.L. Muhich, B.D. Ehrhart, I. Al-Shankiti, B.J. Ward, C.B. Musgrave, A.W. Weimer, A review and perspective of efficient hydrogen generation via solar thermal water splitting, Wiley Interdiscip. Reviews-Energy Environ. 5 (2016) 261–287.

[4] J. Ditzig, H. Liu, B.E. Logan, Production of hydrogen from domestic wastewater using a bioelectrochemically assisted microbial reactor (BEAMR), Int. J. Hydrogen Energy 32 (2007) 2296–2304.

[5] B.E. Logan, D. Call, S. Cheng, H.V.M. Hamelers, T.H.J.A. Sleutels, A.W. Jeremiasse, R.A. Rozendal, Microbial electrolysis cells for high yield hydrogen gas production from organic matter, Environ. Sci. Technol. 42 (2008) 8630–8640.

[6] B.E. Logan, Scaling up microbial fuel cells and other bioelectrochemical systems, Appl. Microbiol. Biotechnol. 85 (2010) 1665–1671.

[7] P.D. Vaidya, E.Y. Kenig, Gas-liquid reaction kinetics: a review of determination methods, Chem. Eng. Commun. 194 (2007) 1543–1565.

[8] R. Kaur, M. Ramakrishna, K.D.P. Nigam, Role of dispersed phase in gas-liquid reactions: a review, Rev. Chem. Eng. 23 (2007) 247–300.

[9] R. Dittmeyer, K. Svajda, M. Reif, A review of catalytic membrane layers for gas/liquid reactions, Top. Catal. 29 (2004) 3–27.

[10] E.W. Egan, C.W. Tobias, Measurement of interfacial re-equilibration during hydrogen bubble coalescence, J. Electrochem. Soc. 141 (1994) 1118–1126.

[11] D.M. Li, Coalescence between small bubbles: effects of surface tension gradient and surface viscosities, J. Colloid Interface Sci. 181 (1996) 34–44.

[12] V.V. Yaminsky, S. Ohnishi, E.A. Vogler, R.G. Horn, Stability of aqueous films between bubbles. Part 2. Effects of trace impurities and evaporation, Langmuir 26 (2010) 8075–8080.

[13] R.G. Rice, Analytical solutions for film thinning dynamics in bubble coalescence, Aiche J. 52 (2006) 1621–1622.

[14] J.P. Munro, C.R. Anthony, O.A. Basaran, J.R. Lister, Thin-sheet flow between coalescing bubbles, J. Fluid Mech. 773 (2015).

[15] C.R. Anthony, P.M. Kamat, S.S. Thete, J.P. Munro, J.R. Lister, M.T. Harris, O.A. Basaran, Scaling laws and dynamics of bubble coalescence, Phys. Rev. Fluids 2 (2017).

[16] J. Eggers, J.R. Lister, H.A. Stone, Coalescence of liquid drops, J. Fluid Mech. 401 (1999) 293–310.

[17] J.D. Paulsen, R. Carmigniani, A. Kannan, J.C. Burton, S.R. Nagel, Coalescence of bubbles and drops in an outer fluid, Nat. Commun. 5 (2014).

[18] M.M. Wu, T. Cubaud, C.M. Ho, Scaling law in liquid drop coalescence driven by surface tension, Phys. Fluids 16 (2004) L51–L54.

[19] S.T. Thoroddsen, T.G. Etoh, K. Takehara, N. Ootsuka, On the coalescence speed of bubbles, Phys. Fluids 17 (2005).

[20] R.L. Stover, C.W. Tobias, M.M. Denn, Bubble coalescence dynamics, Aiche J. 43 (1997) 2385–2392.

[21] Y. Kim, S.J. Lim, B. Gim, B.M. Weon, Coalescence preference in densely packed microbubbles, Sci. Rep. 5 (2015).

[22] B.M. Weon, J.H. Je, Coalescence preference depends on size inequality, Phys. Rev. Lett. 108 (2012).

[23] R. Chen, H.D. Yu, L.K. Zhu, R.M. Patil, T. Lee, Spatial and temporal scaling of unequal microbubble coalescence, Aiche J. 63 (2017) 1441–1450.

[24] F.H. Zhang, S.T. Thoroddsen, Satellite generation during bubble coalescence, Phys. Fluids 20 (2008).

[25] Y. Cao, J. Bontrager-Singer, L. Zhu, A 3D microfluidic device fabrication method using thermopress bonding with multiple layers of polystyrene film, J. Micromech. Microeng. 25 (2015).

[26] L. Zhu, N. Kroodsma, J. Yeom, J.L. Haan, M.A. Shannon, D.D. Meng, An on-demand microfluidic hydrogen generator with self-regulated gas generation and self-circulated reactant exchange with a rechargeable reservoir, Microfluid. Nanofluid. 11 (2011) 569–578.

[27] J.S. Lee, B.M. Weon, J.H. Je, X-ray phase-contrast imaging of dynamics of complex fluids, J. Phys. D-Appl. Phys. 46 (2013).

[28] F. Behroozi, A. Perkins, Direct measurement of the dispersion relation of capillary waves by laser interferometry, Am. J. Phys. 74 (2006) 957–961.